Controlling the Structural, Mechanical and Frictional Properties of MoSx Coatings by High-Power Impulse Magnetron Sputtering

David Kokalj [1,*] , **Jörg Debus** [2] , **Dominic Stangier** [1] , **Henning Moldenhauer** [2] , **Alexander Nikolov** [3] , **Alexandra Wittig** [1] , **Andreas Brümmer** [3] **and Wolfgang Tillmann** [1]

1   Institute of Materials Engineering, TU Dortmund University, Leonhard-Euler-Straße 2, 44227 Dortmund, Germany; dominic.stangier@tu-dortmund.de (D.S.); alexandra.wittig@tu-dortmund.de (A.W.); wolfgang.tillmann@tu-dortmund.de (W.T.)
2   Experimental Physics 2, TU Dortmund University, Otto-Hahn-Straße 4a, 44227 Dortmund, Germany; joerg.debus@tu-dortmund.de (J.D.); henning.moldenhauer@tu-dortmund.de (H.M.)
3   Chair of Fluidics, TU Dortmund University, Leonhard-Euler-Straße 5, 44227 Dortmund, Germany; alexander.nikolov@tu-dortmund.de (A.N.); andreas.bruemmer@tu-dortmund.de (A.B.)
*   Correspondence: david.kokalj@tu-dortmund.de; Tel.: +49-(0)231-755-4866

check for updates

Abstract: Tribology, as the science and technology of interacting surfaces, typically relies on liquid lubricants which reduce friction and wear. For environmentally friendly tribological purposes and applications requiring a liquid-free performance, solid lubricants, such as MoS_2 coatings, play an essential role. It is crucial to understand the interplay between the parameters of the coating synthesis and the characteristics of the coating. The impact of the deposition parameters on the structural, mechanical and frictional properties of MoS_x thin films, which are synthesized by high-power impulse magnetron sputtering, are studied. The morphology, topography and stoichiometry ($2.02 < x < 2.22$) of the films are controlled by, in particular, the bias-voltage and heating power applied during the sputtering process. In combination with a low pulse frequency the hardness and elastic stiffness of the MoS_x films are enhanced up to 2 and 90 GPa, respectively. This enhancement is assigned to a shortening of the Mo-S bonding lengths and a strengthening in the interatomic coupling as well as to a formation of small-sized crystallites at the surface. The friction coefficient reduces to $\mu = 0.10$ for films with an initial (100) orientation and the mean roughness of the MoS_x films decreases below 15 nm by shortening the cathode pulses.

Keywords: molybdenum disulfide; high power impulse magnetron sputtering; thin films; friction; inelastic light scattering

1. Introduction

Surface modifications of machining parts, subjected to a tribological load, provide the performance and long lifetime which are highly required for today's production processes and technical applications. Wear resistance and reduced friction are achieved by physical-vapor-deposition (PVD) coatings [1,2]. In this context, the rotor contact in dry-running twin-screw machines without timing gears, examined as prototypes in various application areas, are of special interest [3–5]. The rotor mesh is characterized by remarkable tribological requirements taking into account that a lubricating auxiliary fluid is not available. In dry-running operations, a relatively high thermal load occurs in the rotor contact (about 400 °C) underlining the importance of a wear protection coating [6]. In addition to typically used tungsten carbide coatings, a similarly hard diamond-like-carbon wear protection film with a hardness

of 15–25 GPa is exploited [7]. The wear rates achieved are promising, but they are still a subject of ongoing research.

In addition to carbon-based hard coatings, lamellar coatings, including graphite, MoS_2 and WS_2, are successfully used as solid lubricants to reduce the friction coefficient between sliding or rolling surfaces [8,9]. MoS_2 features a lamellar buildup in a hexagonal structure with individual molybdenum and sulfur planes, while the molybdenum layer is surrounded by sulfur at both sides. Within the planes covalent bonds and between the planes easily slidable Van-der-Waals bonds are present [10]. For this reason, the different layers can slide against each other and allow low friction coefficients. Since these tribological properties are preserved up to at least 400 °C, these layers find application in various fields [8,11,12].

In contrast to bulk materials, superior properties are achieved using sputtered MoS_2 layers. These layers provide low coefficients of friction and a long lifetime compared to films grown by other methods, such as powder-compacted layers [13]. MoS_2 layers exhibit a coefficient of friction between $\mu = 0.15$ and 0.30 in conventional air containing at 50% humidity [14]. The coefficient of friction depends on various external parameters, such as the contact pressure, temperature, humidity and layer properties including, for example, the film thickness, growth structure and elastic modulus [8]. The PVD parameters play an essential role for the structural and tribological behavior of MoS_2 films.

Important tribological properties, like the friction coefficient, wear resistance and wear particle formation, depend on the composition, adhesion, and morphology or porosity of the interacting surface [15]. A low coefficient of friction and an extended lifetime shall be achieved by combining a good adhesion of the surface layer to the substrate, a high purity of the coating, and a dense morphology with a small crystallite size [15]. For a HiPIMS grown MoS_x thin film, a decrease of the friction coefficient is reported with an enhanced surface pressure applied during the tribological contact, due to the formation of more third-body particles leading to a thicker tribofilm formation [16]. A transfer film formation is also promoted by oxygen and H_2O in the atmosphere as reported by Li et al. [17].

The growth temperature affects the crystallite size and stoichiometry of the coating: At a temperature of 100 °C, an S/Mo ratio of 1.90 is observed, for direct-current sputtered MoS_x films. The ratio further decreases down to 1.71 at about 300 °C, i.e., with increasing substrate temperature [18]. The influence of the bias-voltage on the stoichiometry and structural properties of MoS_2-Ti composite films has been studied by Bülbül et al. [19]. With an increasing bias-voltage, the layer thickness and the S/Mo ratio are reduced due to resputtering phenomena and an enhanced ion bombardment. According to Vierneusel et al. [20], the usage of a high bias-voltage leads to a decrease in the friction coefficient, but also to a short coating lifetime. This effect may be ascribed to a high kinetic energy of the species due to the increased bias-voltage. Nevertheless, the diverse impacts of the deposition parameters on the coating properties as well as the corresponding microscopic reasons are not understood in detail yet.

MoS_2 thin films have mainly been magnetron-sputtered in the direct-current [18,21] or radio-frequency [20,22–26] mode. To improve the coating properties, MoS_2 composite coatings containing TiN [27], or e.g., Ti [19,28], have been grown. Another attempt is the synthesis of a Mo_2N/MoS_2 composite, merging the unique properties of both materials [29]. Instead of changing the chemical composition, a downstreamed vacuum heat treatment can improve the wear life time of the coating, due to a change from an amorphous-like to a nanocrystal state of the microstructure [30]. A sophisticated growth method is by high-power impulse magnetron sputtering (HiPIMS), which provides a high ionization of the particle plasma by short impulses on the cathode. Films synthesized by HiPIMS reveal a dense and fine morphology [31] leading to a high hardness [32] and a high oxidation resistance [33]. Thus, the tribological properties, like the wear resistance of the film grown by HiPIMS can be improved [34]. Up to now, mainly composite coatings were grown by the HiPIMS method, for example $(Cr_{1-x}Al_x)N+MoS_y$ [35] and pure MoS_x HiPIMS coatings [36,37] have only been rarely

studied. For MoS_x thin films grown in HiPIMS mode, an increase of the bias-voltage leads to a more pronounced (100) orientation accompanied by an decrease of the friction coefficient [37].

For MoS_x films synthesized by the HiPIMS method including the bias-voltage, the impacts of the growth parameters on the structural, mechanical and frictional properties of the films were studied in this research. For comparison, a conventionally direct-current magnetron sputtered MoS_x coating was prepared. For correlating the growth parameters with the MoS_x film properties and providing microscopic descriptions, complementary characterization methods including scanning electron microscopy, X-ray diffraction, laser light scattering, nanoindentation as well as ball-on-disc tribometer experiments were used. It is demonstrated that the structural inhomogeneity of the dense MoS_x films is remarkably affected by the bias-voltage and heating power. An increasing heating power shifts the stoichiometric S/Mo ratio towards 2 which is attributed to a high surface diffusion during the synthetization process. A weak heating power and low pulse frequency lead to a shortening of the Mo-S bonding lengths and to an enhancement in the interatomic coupling as well as to the formation of small-sized crystallites at the surface. As a result, the hardness of the MoS_x films rises up to 2 GPa. The friction coefficients of the HiPIMS films range between 0.10 and 0.16. A high coefficient of friction is observed for films with a homogeneous structure which is resistant against shear forces. A low averaged friction coefficient is achieved for films with an initial (100) orientation. Moreover, short pulses cause smooth surfaces of the MoS_x coatings with mean roughness values of less than 15 nm. The study provides a major step towards the understanding of the interplay between HiPIMS deposition parameters and the properties of MoS_x films, making them a promising platform for the solid lubrication in tribologically relevant applications.

2. Materials and Methods

MoS_x thin films were deposited on heat-treated steel substrates (1.2343, AISI-H11) with a hardness of (8.1 ± 0.4) GPa and on (100)-oriented silicon wafers using an unbalanced magnetron sputtering device (CC800/9 Custom, CemeCon AG, Würselen, Germany). The substrates were ground and polished in different steps (9, 6 and 3 μm suspension) prior to the coating process to enhance the surface quality to an arithmetic mean roughness of $Ra = (4.9 \pm 0.5)$ nm. After each step, the substrates were cleaned in an ultrasonic ethanol bath. In the PVD chamber, the substrates were heated up and were subjected to a gas-etching process (mixture of argon and krypton gas) which removed oxides from the surface. A subsequent booster-etching process using two molybdenum targets was used to improve the adhesion of the MoS_x films on the substrates, as reported for MoS_2-Nb composites [38]. The films were deposited by the HiPIMS technique using a MoS_2 target of 99.5% purity and an average cathode power of 3 kW. The used target arrangement is shown in Figure 1a.

Argon and krypton were used as process gases leading to a total chamber pressure of 350 mPa. The bias-voltage was synchronized with the HiPIMS cathode by 150-μs-pulses and an offset of 40 μs. The heating power was set to $P_H = 3$ kW, the bias-voltage to $U_B = -150$ V, the pulse frequency to $f_P = 700$ Hz, and the pulse duration to $t_P = 150$ μs. These deposition parameters define the central parameters of our coating design and, in turn, that of sample ID1. For the samples ID2 to ID9, the deposition parameters were changed to lower and higher values in a definite manner so that three different values for each parameter were investigated. An overview of the deposition parameters and structural properties is given in Table 1. A reference MoS_x thin film (DC) was sputtered in direct-current mode with deposition parameters corresponding to that of the central sample ID1. For the reference film the bias-voltage was changed from the pulsed to the direct-current mode. For all parameters, the sputtering time was kept constant at 3800 s.
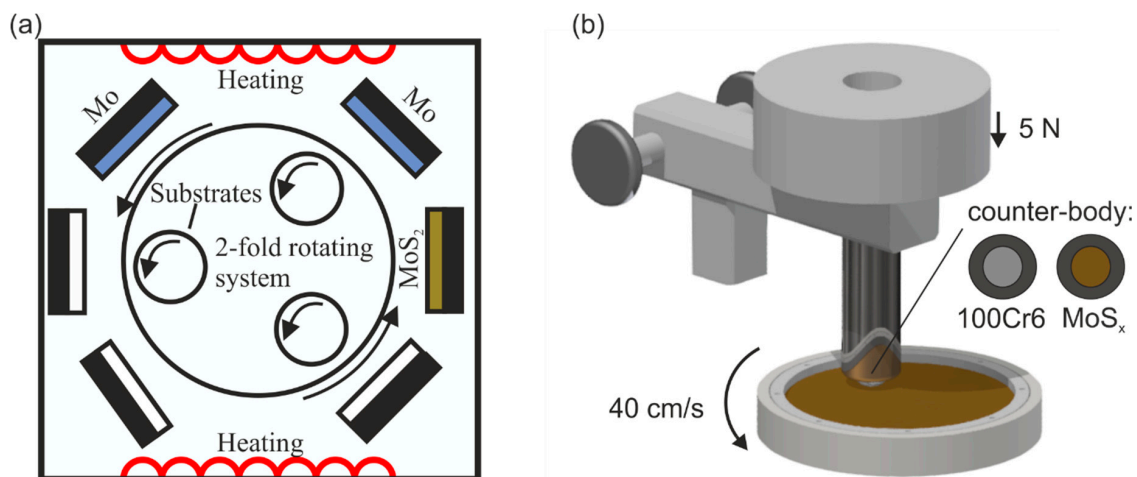
Figure 1. (**a**) Arrangement and target setup in the deposition chamber and (**b**) experimental setup of the ball-on-disc investigations.

Table 1. Overview of the deposition parameters and structural properties of the MoS$_x$ films, including the substrate temperature T_S, coating thickness d, mean roughness Ra and the intensity ratio between the XRD peaks (100) and (002).

ID	P_H (W)	U_B (V)	f_P (Hz)	t_P (µs)	T_S (°C)	d (µm)	Ra (nm)	Mo (at.%)	S (at.%)	S/Mo Ratio	(100)/ (002)
DC	3000	150	–	–	312 ± 1	2.70 ± 0.02	79.1 ± 1.5	38.62 ± 0.25	66.38 ± 0.25	1.59 ± 0.02	7.8 ± 0.4
1	3000	150	700	150	311 ± 5	1.75 ± 0.01	18.6 ± 0.7	33.07 ± 0.22	66.93 ± 0.22	2.02 ± 0.02	2.2 ± 0.1
2	**500**	150	700	150	128 ± 1	1.41 ± 0.01	13.1 ± 1.1	31.02 ± 0.45	68.89 ± 0.45	2.22 ± 0.05	1.2 ± 0.1
3	**5500**	150	700	150	388 ± 5	2.03 ± 0.02	21.6 ± 2.0	32.43 ± 0.30	67.57 ± 0.30	2.08 ± 0.03	1.4 ± 0.1
4	3000	**50**	700	150	308 ± 2	2.26 ± 0.01	22.4 ± 3.2	32.20 ± 0.11	67.80 ± 0.11	2.11 ± 0.01	1.6 ± 0.1
5	3000	**250**	700	150	306 ± 1	1.55 ± 0.02	18.6 ± 3.5	31.54 ± 0.20	68.46 ± 0.20	2.17 ± 0.02	6.7 ± 0.3
6	3000	150	**400**	150	306 ± 1	1.25 ± 0.01	12.7 ± 0.5	31.97 ± 0.32	68.03 ± 0.32	2.14 ± 0.03	1.9 ± 0.1
7	3000	150	**1000**	150	308 ± 1	2.48 ± 0.02	29.3 ± 0.6	32.38 ± 0.16	67.62 ± 0.16	2.09 ± 0.02	9.4 ± 0.1
8	3000	150	700	**85**	306 ± 1	1.47 ± 0.01	16.9 ± 3.3	31.46 ± 0.18	68.54 ± 0.18	2.18 ± 0.02	3.7 ± 0.4
9	3000	150	700	**215**	305 ± 1	2.10 ± 0.02	80.3 ± 3.7	31.77 ± 0.24	68.23 ± 0.24	2.15 ± 0.02	10.6 ± 0.8

The coatings were designed by means of a predictive analytics software (JMP Pro 14, SAS Institute Inc., Cary, NC, USA). For the statistically based analysis of the parameters and experimental data, linear effects of the deposition parameters on structural and mechanical properties of the MoS$_x$ films were taken into account and mutual interactions were neglected. The significance of the analyzed deposition parameters was determined in accordance with a significance level of 0.05 using the probability value (p-value). For evaluating the effects of the deposition parameters, a t-test was performed. The respective values are listed in Table 2. The statistical analysis is based on the following null hypothesis: The deposition parameters (heating power, bias-voltage, pulse frequency and pulse duration) do not affect the properties of the MoS$_x$ films.

Table 2. Statistical evaluation of the effects of the deposition parameters on different film properties using p- and t-values.

Deposition Parameter	p-Value	t-Value	Deposition Parameter	p-Value	t-Value
Roughness			Coating Thickness		
Pulse duration	0.0663	2.51	Pulse frequency	0.0004	11.00
Pulse frequency	0.5500	0.65	Bias-voltage	0.0032	−6.33
Substrate temperature	0.6222	0.53	Substrate temperature	0.0043	5.85
Bias-voltage	0.8908	−0.15	Pulse duration	0.0048	5.68

Table 2. *Cont.*

Deposition Parameter	*p*-Value	*t*-Value	Deposition Parameter	*p*-Value	*t*-Value
S/Mo Ratio			Full width at Half Maximum (FWHM) of (100)-XRD Peak		
Substrate temperature	0.1466	−1.80	Pulse frequency	0.0092	−4.72
Bias-voltage	0.5240	0.70	Substrate temperature	0.0642	−2.54
Pulse frequency	0.5936	−0.58	Bias-voltage	0.1260	1.93
Pulse duration	0.7358	−0.36	Pulse duration	0.1395	−1.84
(100)/(002)-XRD Intensity Ratio			(002)-XRD Peak Position		
Pulse frequency	0.1692	1.68	Substrate temperature	0.0019	7.27
Pulse duration	0.1970	1.55	Pulse frequency	0.0763	2.38
Bias-voltage	0.3160	1.15	Pulse duration	0.4037	−0.93
Substrate temperature	0.6466	0.49	Bias-voltage	0.4382	0.86
Hardness			Friction Coefficient (Uncoated Counter Body)		
Pulse frequency	0.0303	−3.29	Bias-voltage	0.0661	−2.51
Substrate temperature	0.0439	−2.90	Pulse frequency	0.2790	1.25
Pulse duration	0.4471	−0.84	Substrate temperature	0.4365	0.86
Bias-voltage	0.5280	0.60	Pulse duration	0.9976	0.00

The voltage and current of the cathode pulses were recorded during the growth processes in 1 µs steps for the different deposition parameters using an oscilloscope type 1280 (PeakTech, Ahrensburg, Germany).

The topography of the MoS_x film surfaces and the morphology of their cross sections, which were prepared by cryogenic breaking, were analyzed by field-emission scanning electron microscopy (SEM; FE-JSEM 7001, Jeol, Tokyo, Japan). The coating thickness was obtained from the cross-sectional SEM images. Energy-dispersive X-ray spectroscopy (EDS) provided the determination of the film composition which enables the calculation of the Mo/S ratio. The physical structure of the thin films was characterized by X-ray diffraction (XRD; D8 Advance, Bruker, Madison, WI, USA) using a wavelength of $\lambda = 0.154187$ nm (Cu-Kα radiation source). The samples were measured in the Bragg–Brentano geometry. The scanning in the 2θ range was done in progressive steps with a width of $0.035°$ and an exposure time of 0.6 s per step. The evaluation of the (100)/(002) intensity ratio is based on the maximum intensities of the (100) and (002) peaks obtained by Lorentzian fits. The full width at half maximum (FWHM) was also obtained by Lorentzian fits. Additionally, the arithmetic mean roughness *Ra* of the films was measured by means of a confocal white-light microscope (µSurf, NanoFocus, Oberhausen, Germany) and evaluated by the software LeicaMap 8 (Leica Microsystems GmbH, Wetzlar, Germany).

Furthermore, the MoS_x coatings were examined with inelastic laser-light scattering spectroscopy to elaborate acoustic and optical vibrations of the MoS_x lattice. A confocal Raman spectrometer (MonoVista CRS + 750/BX51, S&I GmbH, Warstein, Germany) with a single-frequency laser ($\lambda = 532$ nm) and liquid-nitrogen cooled charge-coupled-device camera was used [6,39]. The laser spot at the sample surface was about 4 µm and the laser power was set to less than 1 mW to exclude laser-induced alterations of the film surfaces.

The hardness and Young's modulus were evaluated from nanoindentation measurements (G200, Agilent Technology, Santa Clara, CA, USA). In total, 49 indents per sample in a distance of 50 µm were performed using a Berkovich diamond tip and the continuous stiffness mode [40,41]. The mechanical properties were measured in a depth between 100 and 500 nm of the MoS_x film to prevent an influence of the surface and the substrate material on the data acquired. A Poisson ratio of $\nu = 0.2$ was assumed [42].

The dependence of the friction coefficient of the MoS_x films on the deposition parameters was studied by ball-on-disc tribometer (CSM-Instruments, Peseux, Switzerland) measurements as visualized in Figure 1b. As counter-body 100Cr6 balls with a diameter of 6 mm, a hardness of $H = (11.31 \pm 0.13)$ GPa, and a Young's modulus of $E = (225.4 \pm 2.3)$ GPa were selected. In addition to

uncoated balls, MoS$_x$ coated counter bodies having the properties of the corresponding samples were used. The friction measurements were conducted at room temperature in air atmosphere containing 50% humidity. The sliding parameters were set to 1500 revolutions, the radius to 8 mm, the velocity to 0.4 m/s and the normal force to 5 N.

3. Results and Discussion

3.1. Structural Properties of the MoS$_x$ Films

The surface topographies and cross-section morphologies of the MoS$_x$ films grown under different HiPIMS deposition parameters are displayed in Figure 2 (top left and right). The thin films demonstrate a fine and dense morphology which in turn indicates a reduced porosity, which is also evaluated from the images of Figure 2. Nevertheless, most of the films reveal a dendritic needle-like structure. A coarse topography, however, characterizes the reference DC sputtered MoS$_x$ film which is comparable to the structure of an RF sputtered MoS$_2$ film [23].
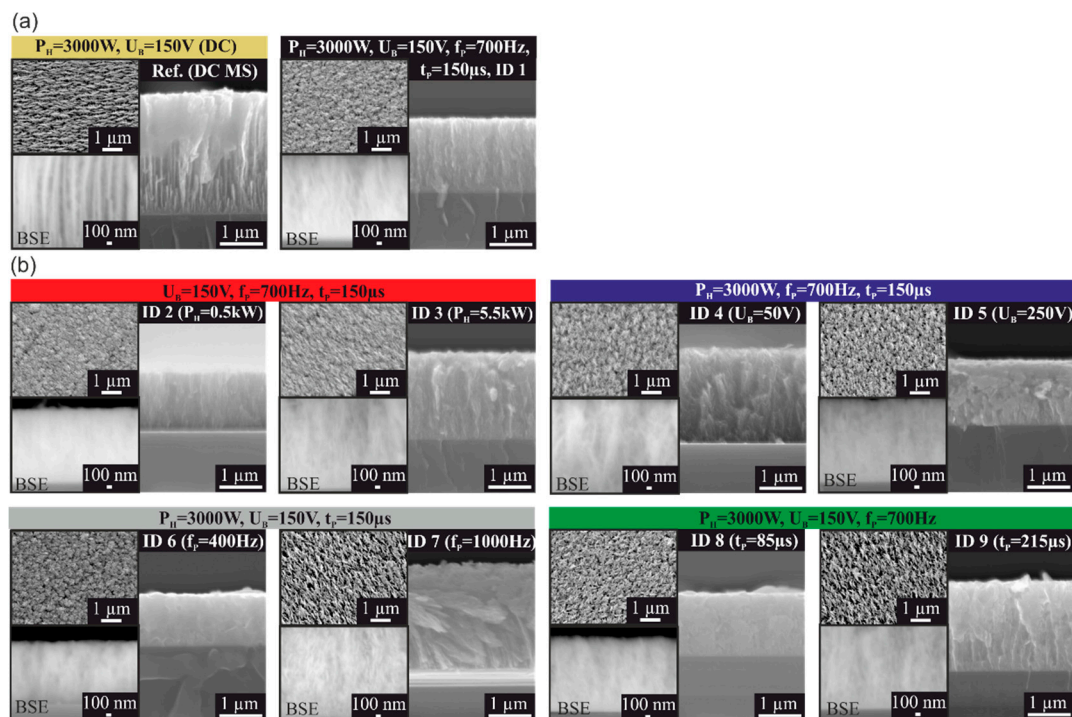

Figure 2. SEM images of the strucutre of (**a**) a DC (yellow) and HiPIMS (black) grown MoS$_x$ thin film and (**b**) HiPIMS grown MoS$_x$ thin films with varied heating power (red), bias-voltage (blue), pulse frequency (grey), and pulse duration (green). The topography of the thin films is shown in the top left inset, and the morphology in the right inset. Magnified cross-section images in backscattered-electron (BSE) mode (bottom left) show details of the morphology.

Further insight into the morphology of the films is provided by high magnified SEM images taken in the backscattered-electron (BSE) mode shown at the bottom left of Figure 2. The growth structure of the films ID8, ID5 and ID2 is more homogeneous than that of the other MoS$_x$ coatings. Hence, we propose that the homogeneity of the HiPIMS film growth becomes pronounced for a short pulse duration, a high bias-voltage, and a low heating power.

The structural quality of the MoS$_x$ film is further elaborated by considering the arithmetic mean roughness *Ra*. According to Table 1, *Ra* varies between (12.7 ± 0.5) (ID6) and (80.3 ± 3.7) nm (ID9), for the films grown by the HiPIMS method. The roughness of the reference DC sample amounts to (79.1 ± 1.5) nm and is comparable to that of ID9. The different deposition parameters do not affect the roughness value significantly according to the statistical evaluation presented in Table 2 (*p*-values

above 0.05). Nevertheless, it is observed that the roughness increases with increasing pulse duration from (16.9 ± 3.3) nm (t_p = 85 μs), to (18.6 ± 0.7) nm (t_p = 150 μs) to (80.3 ± 3.7) nm (t_p = 215 μs), for ID8, ID1 and ID9, respectively. The aforementioned trend to obtain a low surface roughness with temporally narrow pulses corresponds with the SEM data on the morphology and topography of homogeneous MoS$_x$ films. Accordingly, the ID8 sample with a smooth surface (*Ra* ~ 17 nm) grown at t_p = 85 μs has a more homogeneous structure than the MoS$_x$ coatings deposited at higher pulse durations.

The cross-section SEM images moreover indicate that the deposition parameters affect the coating thickness *d* in different ways. These dependences are depicted in Figure 3. A high thickness, deduced from the cross-sectional images, of the MoS$_x$ coatings is achieved with increasing heating power, pulse duration and frequency. This trend is also indicated by the positive *t*-values in Table 2. Increasing the absolute value of the negative bias-voltage (*t*-value < 0) leads to a narrowing of the MoS$_x$ film. For instance, the lowest thickness *d* = (1.25 ± 0.01) μm and the highest one *d* = (2.48 ± 0.02) μm are obtained for the ID6 and ID7, respectively. The thickness of the reference coating amounts to (2.70 ± 0.02) μm, see Table 1. According to the statistical evaluation, see Table 2, the pulse frequency and bias-voltage exhibit the highest impact on the coating thickness. Furthermore, the substrate temperature T_S defined by the heating power is important for controlling the coating thickness; considering the samples ID2 and ID3, a high substrate temperature is related to a large coating thickness.
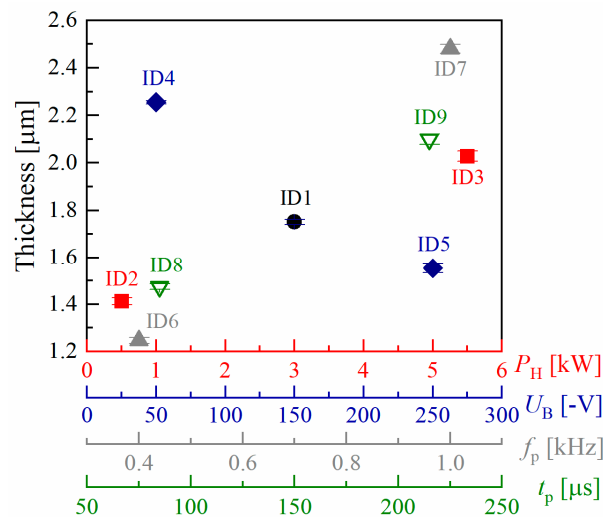

Figure 3. Dependence of the thickness of the HiPIMS MoS$_x$ films on the heating power P_H and bias-voltage U_B, for f_p = 0.7 kHz and t_p = 150 μs, as well as the pulse frequency f_p and pulse duration t_p, for P_H = 3 kW and U_B = −150 V.

The film-thickness dependence is additionally studied by the impact of the peak current density on the deposition rate. Papa et al. [43] ascribed a lowering of the deposition rate and coating thickness to an increased peak current density. For Cr sputtering, an increase in the deposition rate is observed with rising peak current density only up to a threshold value of about 570 mA/cm^2 [44]. For higher densities, the deposition rate decreases owing to self-sputtering effects. To calculate the maximum peak current density, the oscilloscope data were taken and the measured maximum current of the individual pulses associated with the target size of (500 × 88) mm^2. Taking into account exemplarily the films ID5 (f_p = 700 Hz, U_B = −250 V) and ID7 (f_p = 1000 Hz, U_B = −150 V), the maximum peak current density is (658 ± 9) mA/cm^2 (ID5) and (543 ± 7) mA/cm^2 (ID7). Indeed, the coating ID5 is about 0.9 μm thinner than that of ID7. A narrowing of the MoS$_x$ film thickness may be caused not only by a self or resputtering for peak current densities above a threshold value, but also by a densification of the film resulting from a high bias-voltage. The latter aspect has been shown within the analysis of the SEM images and was observed in MoS$_x$ [37] and MoS$_2$-Ti films [19].

The ratio between the Mo and S atoms within the MoS_x films was evaluated from EDS measurements of the chemical composition. As listed in Table 1, the HiPIMS grown MoS_x films exhibit S/Mo ratios between 2.02 ± 0.02 (ID1) and 2.22 ± 0.05 (ID2), which are higher than that of an MoS_2 alloy. Accordingly, the sulfur content of all HiPIMS grown films is higher than 66.6 at.%. A lower ratio of 1.59 ± 0.02 is measured for the DC sputtered film. The change from the DC to the HiPIMS growth method demonstrates the highest influence on the stoichiometry of the MoS_x films from 1.59 to 2.13 on average, although both methods used the same average cathode power. This leads to the conclusion that the ionization of the sputtered material by using different power supplies plays a superordinate role. Among the HiPIMS films the increase in the substrate temperature, caused by an enhanced heating power, seems to reduce the S/Mo ratio towards 2. By increasing the substrate temperature from 100 to 300 °C a decrease of the S/Mo ratio from 1.90 to 1.71 is reported for DC sputtered thin films [15]. S/Mo ratios between 0.8 and 1.5 are obtained for bipolar pulsed magnetron sputtered MoS_x thin films [45]. According to reference [16], an increasing bias-voltage results in a reduction of the S/Mo ratio due to resputtering and an enhanced ion bombardment. These effects are most likely to be found in the resputtering of sulfur since it has a lower atomic mass than molybdenum. Therefore, we attribute an appearance of selective resputtering of sulfur atoms to the DC sputtered reference sample. The constant resputtering in case of the direct-current-bias leads to a higher selective resputtering due to the higher duty cycle compared to the synchronized-pulsed bias of the HiPIMS processes.

The XRD spectra of the MoS_x films are shown in Figure 4a,b. Several peaks are observed in the analyzed 2θ-range. The diffraction peaks at about 44° and 64° stem from the 100Cr6 substrate, while the other Bragg peaks are attributed to diffractions from the (002), (100), (101) and (110) planes of MoS_x. The presence of such a number of peaks indicates that the films reveal a polycrystalline structure [46]. Moreover, for MoS_x coatings with $x > 1.3$, the formation of a hexagonal atomic arrangement has the highest probability [18]. A regular atomic arrangement manifests itself in narrow peak linewidths. The diffraction peaks of the MoS_x films are quite broad. The broadening results from either an increase in the residual strain, leading to an imperfect crystalline ordering within the films, or a size narrowing of crystallites formed at the surface [47]. The latter aspect is governed by the Scherrer equation $D = K\lambda/(\beta \cos\theta)$ which relates the average crystallite size D with the diffraction angle θ, the excitation wavelength λ, the shape factor $K = 0.89$ and the full width at half maximum (FWHM) denoted by β [48]. For the (100) peak, the mean crystallite size is given by (9.4 ± 1.0) nm.
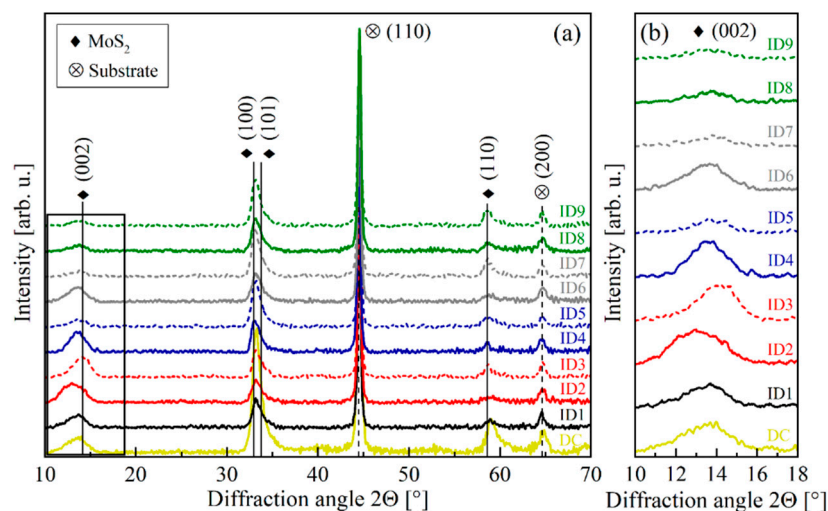

Figure 4. (**a**) XRD spectra of the HiPIMS and DC sputtered MoS_x films. (**b**) Detailed view on the shifts of the (002)-MoS_2 Bragg peak.

Due to broadening, the (100) and (101) diffraction peaks of MoS_x overlap with each other at about $2\Theta = 33.2°$, for most films. The FWHM of the intense (100) peak is shown in Figure 5a as function of

the deposition parameters. A considerable decrease in the FWHM is observed with increasing the pulse frequency; the *p*-value is given by 0.0092 (see Table 2). For instance, the FWHM of the (100) peak of ID6 (400 Hz) amounts to 1.03° ± 0.05°, while it is 0.86° ± 0.04° for ID7 (1000 Hz). An enhanced pulse frequency in a HiPIMS film synthetization is connected to the transfer of a large number of atoms with high kinetic energies to the sample. During the nucleation process of these mobile atoms they lose energy in a specific time. Changing the pulse frequency alters the dynamics including atomic collisions and the energy dissipation of the atoms at the surface. For a high pulse frequency, a large number, i.e., a sea of high-kinetic Mo and S atoms is present at the surface. In this collective state the atoms take such lattice positions that the surface energy is minimized [49]. As a result, the atoms form a quite crystalline lattice which is indicated by a small XRD-peak FWHM. In turn, the increase in the substrate temperature gives rise to a narrowing of the (100) peak. Moreover, the high kinetic energy and mobility of the Mo and S atoms at the surface may result in a reduced internal strain and, respectively, in the formation of large-sized crystallites. In particular, the former aspect agrees with the observation that, for a high substrate temperature, the stoichiometry ratio of $x = 2$ for MoS_x is realized. This is assigned to a high surface diffusion during the growth process, and to a relaxation of strain within the MoS_2 film.
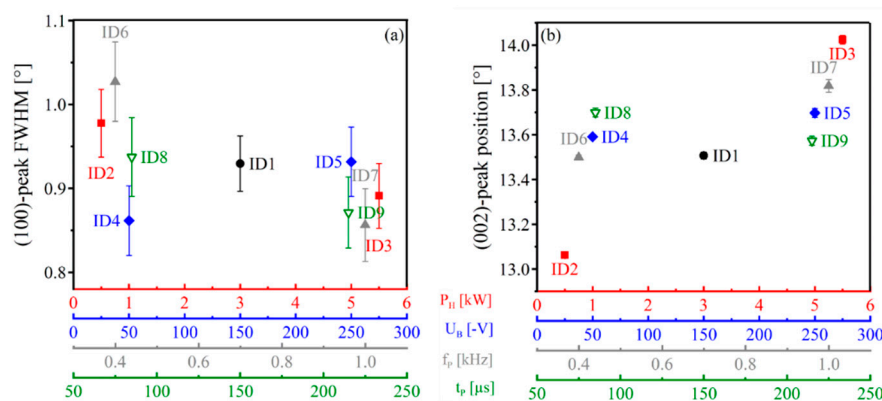

Figure 5. Dependence of the (**a**) (100)-XRD-peak full width at half maximum (FWHM) and (**b**) (002)-peak position on the heating power P_H and bias-voltage U_B, for $f_P = 0.7$ kHz and $t_P = 150$ μs, as well as the pulse frequency f_P and pulse duration t_P, for $P_H = 3$ kW and $U_B = -150$ V. In (**b**) the absolute error does not exceed the symbol size.

By comparison, the (002) peak shows a wide broadening in most of the MoS_x films, see Figure 5b. For an increasing bias-voltage, for example, the diffraction peak changes from a symmetric, pronounced profile (ID4) to a weak (ID1) and negligible (ID5) shape. The (002) peak indicates the presence of a well-stacked layered structure along the (002) crystal direction [50]. The shift in the position of the (002) peak (see Figure 5b) is attributed to a change in the distance between the atomic layers along the (002) stacking. Since the Bragg diffraction angle is inversely proportional to the distance, the distance between the stacked layers is enlarged for ID2 ($2\Theta = 13.07° ± 0.01°$) and ID4, while it becomes smaller, in particular for ID3 ($2\Theta = 14.04° ± 0.02°$). An increase in the heating power, as indicated by a large positive *t*-value for the substrate temperature in Table 2, causes a shift of the (002) peak to large diffraction angles: the spacing between the layers along the (002) direction becomes smaller. Since a high heating power or high substrate temperature significantly drives the S/Mo ratio towards 2, fewer sulfur atoms are arranged within the layers so that the interlayer spacing is reduced.

Considering the intensities of the (002) and (100) peaks, we see that the (100)/(002) intensity ratio differs strongly among the MoS_x films. For the samples ID9, ID7 and ID5 the ratio is large, see Table 1; thus, these films are predominantly (100)-oriented. The XRD patterns of the other films are contributed by the (101) peak and a broad (002) peak which furthermore shifts in its position. Interestingly, neither

the surface roughness nor the coating thickness can be correlated to the preferential film orientation along the (100) direction.

The inelastic light-scattering spectra of the different MoS$_x$ HiPIMS coatings and of a mechanically exfoliated MoS$_2$ monolayer are shown in Figure 6. In panel (a) the disorder-induced acoustic-phonon lines at about 150, 180 and 230 cm^{-1} are depicted [51], while in panel (b) the E$_{2g}^1$ Raman mode at about 376 cm^{-1}, the A$_{1g}$ mode at about 405 cm^{-1}, and the weak 2LA(M) mode at about 450 cm^{-1} are observed [52].
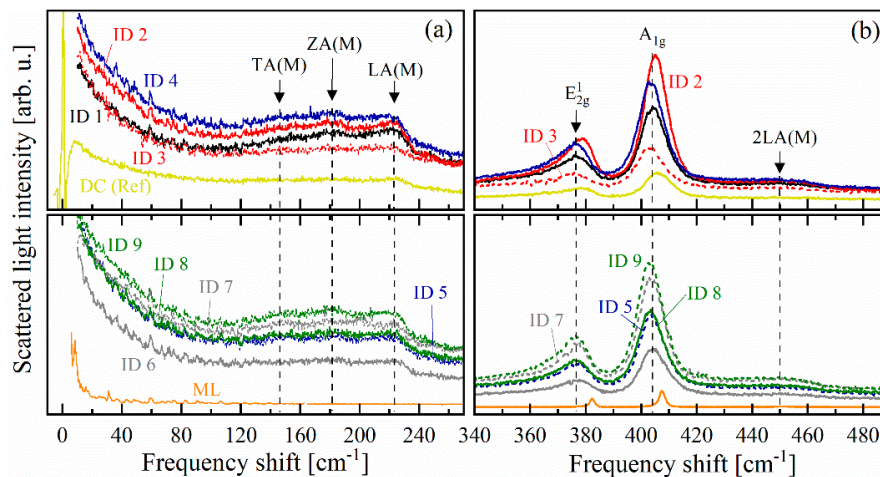
Figure 6. Inelastic light scattering spectra of the MoS$_x$ films and a mechanically exfoliated MoS$_2$ monolayer (ML). In (**a**) the acoustic phonon modes at about 180 cm^{-1} and in (**b**) the optical phonon modes at about 390 cm^{-1} are depicted. The laser line at 0 cm^{-1} is shown exemplarily in the spectrum of the DC sputtered film. These Stokes scattered lines were collected with an integration time of 100 s. Each film was studied at three different surface positions. The spectrum of the monolayer (ML) is multiplied by 1/100.

In comparison to the mean spectral positions of the A$_{1g}$ and E$_{2g}^1$ modes indicated by the vertical dashed lines in Figure 6b, the modes shift to lower frequencies for ID3 and, in particular, to higher frequencies for ID2. The main difference between these HiPIMS films is the different heating powers used. The low- (high-)frequency shift occurs for the MoS$_x$ film grown by a high (low) heating power. In turn, this correlation can be transferred to the substrate temperature. The E$_{2g}^1$ (A$_{1g}$) phonon mode describes an in-plane (out-of-plane) vibration of Mo and S atoms [53]. The scattering frequency is generally connected via $\Delta E \propto \sqrt{W}/\left(l \sqrt{m}\right)$ to the bonding length l and the interaction strength W between the atoms with effective mass m. Based on the frequency shifts, we assume that with increasing heating power or, respectively, substrate temperature, the bonding become longer and, in turn, the coupling strength decreases. It is in agreement with the behavior that at a high temperature and, respectively, large thermal energy, the lattice becomes relaxed. The relaxation results in a bond length adjustment/adaption with respect to the equilibrium (electrostatic) atomic positions. Since these lattice vibrations are not connected to the interlayer spacings, the inelastic light scattering results shall not be brought into relation to the XRD results concerning the (002) diffraction peak.

The linewidths of the optical phonon modes at about 390 cm^{-1} and the acoustic phonons at about 180 cm^{-1} are broad for all films studied. They are broader than the typically observed lines in MoS$_2$ layered structures or bulk crystals [36,54] and in HiPIMS MoS$_x$ films [36,54]. On the one hand, the broadening may be assigned to a non-uniform stoichiometric ratio of the Mo and S atoms. The variation in the coordination and termination of the bonding thus increases the dispersion of the scattering frequencies. On the other hand, the line broadening may be related to the degree of non-single crystallinity of the MoS$_x$ coatings. Accordingly, the bonds between the Mo and S atoms have different lengths and coupling strengths.

For ID1, ID2 and ID9 (see Figure 6a) the acoustic phonon modes are quite pronounced. They were grown at the low and central heating power or, respectively, at large pulse duration. We assume that the slight sharpening of the acoustic phonon modes indicates a reduced inhomogeneity in the structural composition of the HiPIMS coatings. The lattice could be arranged in a slightly more uniform way and the spatial distribution of the crystallite sizes may be more homogeneous. This assumption would agree with the aforementioned characterization results for the respective MoS_x films.

In comparison to the scattering spectrum of the MoS_2 monolayer (see the orange curve in Figure 6) the optical phonon modes are shifted—to low frequencies on the whole. Actually, for micrometer-thin MoS_2 layers, the E_{2g}^1 (A_{1g}) Raman line shifts to lower (higher) frequencies, so that the spectral distance between the peaks enlarges [54]. Here, both Raman lines shift however to low frequencies. This behavior is probably due to the adsorption of nitrogen since a surface coverage of about 10% nitrogen yields a shift of about -7 cm^{-1} of both lines [55].

3.2. Mechanical and Tribological Properties

The hardness and Young's modulus are also studied in dependence on the HiPIMS deposition parameters. In Figure 7 the hardness of the different MoS_x films are shown as functions of the heating power, bias-voltage, pulse frequency and duration. Since Young's modulus behaves similarly, it is not graphically demonstrated. Table 3 lists the hardness H and elastic modulus E values as well as their ratios, which only slightly differ from each other. A clear dependence of the hardness on the heating power and pulse frequency is indicated in Figure 7. The hardness of the MoS_x films is enhanced from less than 0.5 to 2 GPa by lowering the heating power/substrate temperature and pulse frequency. In detail, the hardness of the films varies between (0.3 ± 0.1) GPa, for ID7, and (2.2 ± 0.1) GPa, for ID6. The Young's modulus varies between (31.5 ± 4.2) GPa for ID7, and (90.3 ± 8.6) GPa for ID6. Accordingly, the H/E ratio of the coatings ranges between 0.010 and 0.025. For direct-current unbalanced magnetron sputtered MoS_2 thin films, an increase in the hardness was related to a low substrate temperature [56], and hardness (Young's modulus) values between 0.2 (15.6 GPa) [23] and 2.0 GPa (51.1 GPa) [56] were reported.
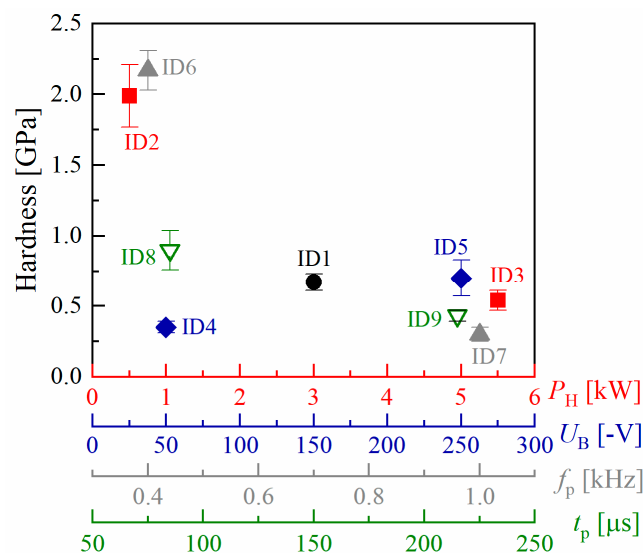
Figure 7. Dependence of the hardness of the HiPIMS MoS_x films on the heating power P_H and bias-voltage U_B, for f_P = 0.7 kHz and t_P = 150 μs, as well as the pulse frequency f_P and pulse duration t_P, for P_H = 3 kW and U_B = −150 V.

Table 3. Mechanical properties (hardness *H* and Young's modulus *E*) and friction coefficient μ of the MoS$_x$ films using the uncoated or MoS$_x$-coated 100Cr6 counter body (cb).

ID	*H* (GPa)	*E* (GPa)	*H/E* Ratio	μ 100Cr6 cb	μ MoS$_x$ cb
DC	0.4 ± 0.1	33.7 ± 3.1	0.012 ± 0.001	0.05 ± 0.01	0.10 ± 0.03
1	0.7 ± 0.1	50.9 ± 3.4	0.013 ± 0.001	0.13 ± 0.01	0.14 ± 0.02
2	2.0 ± 0.2	78.8 ± 8.8	0.025 ± 0.004	0.12 ± 0.02	0.11 ± 0.01
3	0.5 ± 0.1	41.6 ± 3.9	0.013 ± 0.001	0.15 ± 0.05	0.18 ± 0.08
4	0.4 ± 0.1	28.6 ± 2.6	0.012 ± 0.001	0.16 ± 0.03	0.14 ± 0.03
5	0.7 ± 0.1	47.4 ± 6.9	0.015 ± 0.001	0.10 ± 0.02	0.09 ± 0.01
6	2.2 ± 0.1	90.3 ± 8.6	0.024 ± 0.002	0.10 ± 0.02	0.10 ± 0.02
7	0.3 ± 0.1	31.5 ± 4.2	0.010 ± 0.001	0.13 ± 0.02	0.13 ± 0.02
8	0.9 ± 0.1	60.1 ± 7.2	0.015 ± 0.002	0.11 ± 0.02	0.10 ± 0.02
9	0.4 ± 0.1	39.9 ± 2.9	0.011 ± 0.001	0.11 ± 0.02	0.12 ± 0.03

The elastic modulus and, in turn, the hardness of a polar covalent material depends merely on the ionicity and bonding length [57]. MoS$_2$ is a polar covalent material, since the difference between the electronegativities of Mo with X_{Mo} = 2.16 and S with X_S = 2.58 exceeds 0.4, for a single bonding. The ionicity *I* is proportional to $1 - \exp\left[-\frac{(X_A - X_B)^2}{4}\right]$; for the hardness, the relation $H \propto \exp(-1.2\,I)/l^{2.5}$ was evaluated [57]. A small ionicity, given for a small electronegativity difference, leads to a large hardness value assuming that the bonding length *l* remains constant. This is in agreement with the fact that covalent bonds typically have a higher hardness than ionic bonds [58]. For the MoS$_x$ films, the stoichiometry ratio S/Mo is often larger than 2. Thus, the larger number of sulfur atoms polarize the Mo-S bonding more strongly, endowing the molybdenum atoms with more positive charge than the sulfur atoms, and both the electronegativity difference as well as *I* increase. As a result, most of the MoS$_x$ films studied exhibit small hardness values. Only the thin films ID2 and ID6 deviate from this observation. The ID2 film was grown at a low substrate temperature and, on basis of the Raman scattering results, the Mo-S bonding length *l* is short. Since the hardness scales with $l^{-2.5}$, the distance shortening between the Mo and S atoms plays an important role for this coating. For ID6, the presence of small crystallites has been deduced from the XRD data. Small crystallites with sizes in the 10 nm range lead to a high elastic stiffness and hardness in accordance with the Hall–Petch strengthening [59].

The friction coefficients of the thin films were obtained by ball-on-disc experiments in order to analyze the influence of the HiPIMS deposition parameters on the suitability of the MoS$_x$ coatings for tribological applications. The friction coefficients of the reference DC and HiPIMS MoS$_x$ films are listed in Table 3. The friction coefficients of the different films do not differ significantly from each other using the uncoated or MoS$_x$-coated 100Cr6 counter body. The friction coefficient *μ* differs from 0.10 ± 0.02 (ID5) to 0.16 ± 0.03 (ID4) using the uncoated counter body, while *μ* changes between 0.09 ± 0.01 (ID5) and 0.16 ± 0.05 (ID3), for the coated counter body. The lowest friction coefficient is shown by ID5. In comparison to that, for the DC sputtered reference film the friction coefficients amount to only 0.05 ± 0.1 against 100Cr6 and 0.10 ± 0.03 against MoS$_x$. For magnetron sputtered MoS$_2$ films, friction coefficients ranging between 0.11 and 0.22 are typically reported [22,56]. The friction coefficient is strongly influenced by the chemical composition and hardness of the coatings [18]. According to Aubert et al. the minimum friction coefficient could be obtained for S/Mo ratios between 1.5 and 1.6 [18]. The low friction coefficient may be ascribed to the basal (002) orientation within the MoS$_x$ film [20,36].

Taking exemplarily film ID5 into account, linear correlations between the coefficient of friction and the most significant structural properties are calculated and displayed in Figure 8. The properties are given by the (100)/(002) XRD-peak intensity ratio (p = 0.0001, t = −17.26), the XRD-(100)-peak FWHM (p = 0.0001, t = −15.48), the hardness (p = 0.0025, t = −6.74) and the S/Mo ratio (p = 0.0057, t = −5.41). An increase in the (100)/(002) intensity ratio, the (100)-peak FWHM and the S/Mo ratio, and a decrease in the hardness is related to a reduction in the friction coefficient. These linear correlations indicate that the friction coefficient depends on several structural and mechanical properties of the MoS$_x$ film.

Moreover, the dependences on the FWHM and S/Mo ratio agree with the experimentally obtained data that, for a high substrate temperature and/or pulse frequency, an XRD line narrowing and a shift of the S/Mo ratio towards 2 are achieved. It is attributed to decreasing the degree of inhomogeneity within the MoS_x material. Accordingly, for a more homogeneous structure, the resistance against, for instance, shear forces is enhanced so that the coefficient of friction rises.
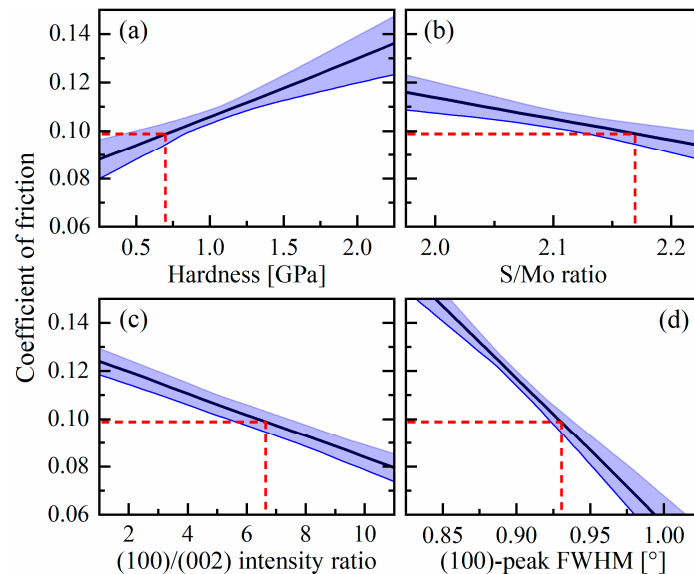
Figure 8. Impacts of significant film properties, (**a**,**b**), as well as XRD characteristics, (**c**,**d**), on the friction coefficient of the MoS_x films, with the uncoated 100Cr6 counter body. The values marked by the red dashed lines belong to ID5.

The correlation $\mu \leftrightarrow (100)/(200)$ (see Figure 8c) shows that a higher intensity of the (002) XRD peak compared to that of the (100) peak, corresponding to a lower (100)/(002) intensity ratio, causes an increase in the friction coefficient. This is contrary to published studies. Generally, a small friction coefficient is observed for magnetron sputtered films showing a basal (002) orientation [36,60]. Didziulis et al. [61] worked out that only the initial friction coefficient depends on the film orientation, since the basal orientation is formed during the tribological contacts and can lead to even lower friction values than a film with initial basal (002) orientation. Concerning the HiPIMS films, a low averaged friction coefficient is achieved for films with a high initial (100) orientation. Accordingly, it seems that, also, the dense microstructure of the HiPIMS films allows tribologically stressed surface areas to change their orientation along the basal (002) direction, as shown in a previous study [37]. Furthermore, an initial (100)-orientation may enhance this process.

4. Conclusions

In summary, the coatings grown by the HiPIMS method demonstrate a fine and dense topography in comparison to the DC sputtered MoS_x film. For a high bias-voltage and low heating power, a reduction in the structural inhomogeneity is observed. A high bias-voltage further causes a narrowing of the MoS_x film thickness probably due to a resputtering process. A weak heating power leads to a shortening of the Mo-S bonding lengths and an enhancement in the interatomic coupling, for in-plane and out-of-plane lattice vibrations. Increasing the heating power shifts the stoichiometric S/Mo ratio towards 2 which may be attributed to a high surface diffusion during the growth process. A high substrate temperature also gives rise to a reduction in the interlayer spacing along the (002) direction of the polycrystalline MoS_x films. The broadening of the phonon modes in the scattered light spectra underlines the non-uniform stoichiometric ratio of the Mo and S atoms and the polycrystalline character of the HiPIMS coatings, which is also demonstrated by the XRD measurements. The XRD data additionally reveal that a high pulse frequency and substrate temperature are related to a diffraction line narrowing.

From the microscopic point of view, changing the pulse frequency alters the dynamics including atomic collisions and the energy dissipation of the atoms at the surface. A large number of high-kinetic Mo and S atoms are present at the surface, and the atoms take such lattice positions that the surface energy is minimized. In this collective state a self-organized growth process occurs, like for nanocomposite films [62], so that large crystallites are formed at the surface thus reducing the internal strain. For large pulse frequencies, thick MoS_x films are grown which are characterized by a reduced densification. Temporally narrow pulses create smooth surfaces of the MoS_x coatings with mean roughness values of less than 15 nm. In comparison to that, the DC sputtered reference sample demonstrates a coarse structure and large thickness.

With respect to the mechanical and tribological properties, it is shown that the hardness of the MoS_x films is enhanced from about 0.5 to 2 GPa by lowering the heating power/substrate temperature and pulse frequency. For the films with the highest hardness values it is proposed that the Mo-S bonding length is short and that small-sized crystallites at the surface lead to a high elastic stiffness. The friction coefficients of the HiPIMS films ranging from 0.10 to 0.16 are not significantly affected by the deposition parameters. However, an impact is deduced from specific coating properties, i.e., the (100/002)-XRD-peak intensity ratio, (100)-XRD-peak linewidth, hardness and S/Mo ratio. It is proposed that, for a more homogeneous structure, the resistance against shear forces is enhanced so that the coefficient of the friction is increased. A low averaged friction coefficient is achieved for films with an initial (100) orientation. Therefore, the dense microstructure of the HiPIMS films allows tribologically stressed surface areas to change their orientation along the basal (002) direction, and an initial (100)-orientation may enhance this process.

Author Contributions: Conceptualization, D.K.; validation, D.S.; investigation, D.K., H.M. and A.W.; writing—original draft preparation, D.K., J.D. and A.N.; writing—review and editing, D.S., A.B. and W.T.; supervision, A.B. and W.T.; funding acquisition, W.T., A.B. and J.D. All authors have read and agreed to the published version of the manuscript.

Conflicts of Interest: The authors declare no conflict of interest.

References

1. Brecher, C.; Spachtholz, G.; Bobzin, K.; Lugscheider, E.; Knotek, O.; Maes, M. Superelastic (Cr,Al)N coatings for high end spindle bearings. *Surf. Coat. Technol.* **2005**, *200*, 1738–1744. [CrossRef]

2. Mattox, D.M. *Handbook of Physical Vapor Deposition (PVD) Processing*, 2nd ed.; William Andrew: Oxford, UK, 2010; ISBN 9780815520375.

3. Janicki, M.; Temming, J.; Kauder, K.; Brümmer, A. Simulationsgestützte Entwicklung eines unsynchronisierten Schraubenladers. In *(Hrsg.): Motorprozesssimulation und Aufladung II. Haus der Technik Fachbuch Band 83*; Pucher, H., Kahrstedt, J., Eds.; Expert-Verlag: Tübingen, Germany, 2007; pp. 146–168.

4. Nikolov, A.; Nadler, K.; Brümmer, A. Experimental and theoretical investigation of screw machines as vacuum blowers. In Proceedings of the 7th International Conference on Compressors and their Systems 2011, City University London, UK, 5–6 September 2011; Elsevier Science: Oxford, UK, 2011; pp. 359–374, ISBN 0857095358.

5. Nikolov, A.; Brümmer, A. Investigating a Small Oil-Flooded Twin-Screw Expander for Waste-Heat Utilisation in Organic Rankine Cycle Systems. *Energies* **2017**, *10*, 869. [CrossRef]

6. Moldenhauer, H.; Bayer, M.; Debus, J.; Nikolov, A.; Brümmer, A. Raman scattering study of micrometer-sized spots of magnetite and hematite formed at 18CrNiMo7-6 screw rotor surfaces due to liquid-free, unsynchronized operation. *IOP Conf. Ser. Mater. Sci. Eng.* **2018**, *425*, 12016. [CrossRef]

7. Grieb, M.; Brümmer, A. Design and examination of a small-scale screw expander for waste heat recovery. In Proceedings of the International Conference on Screw Machines 2014, TU Dortmund University, Germany, 23–24 September 2014; VDI-Verl.: Düsseldorf, Germany, 2014; pp. 197–210, ISBN 978-3-18-092228-7.

8. Holmberg, K.; Matthews, A. *Coatings Tribology. Properties, Mechanisms, Techniques and Applications in Surface Engineering*; Elsevier Professional: Oxford, UK, 2009; ISBN 978-0-444-52750-9.

9. Wong, K.C.; Lu, X.; Cotter, J.; Eadie, D.T.; Wong, P.C.; Mitchell, K.A.R. Surface and friction characterization of MoS_2 and WS_2 third body thin films under simulated wheel/rail rolling–sliding contact. *Wear* **2008**, *264*, 526–534. [CrossRef]

10. Wang, Z.M. *MoS2: Materials, Physics, and Devices*; Lecture Notes in Nanoscale Science and Technology; Springer: Cham, Switzerland, 2014; Volume 21, ISBN 9783319028507.

11. Davim, J.P. *Tribology of Nanocomposites*; Springer: Berlin/Heidelberg, Germany, 2013; ISBN 9783642338816.

12. Charoo, M.S.; Wani, M.F.; Hanief, M.; Rather, M.A. Tribological Properties of MoS_2 Particles as Lubricant Additive on EN31 Alloy Steel and AISI 52100 Steel Ball. *Mater. Today Proc.* **2017**, *4*, 9967–9971. [CrossRef]

13. Roberts, E.W. Ultralow friction films of MoS_2 for space applications. *Thin Solid Films* **1989**, *181*, 461–473. [CrossRef]

14. Nabot, J.-P.; Aubert, A.; Gillet, R.; Renaux, P. Cathodic sputtering for preparation of lubrication films. *Surf. Coat. Technol.* **1990**, *43–44*, 629–639. [CrossRef]

15. Fleischauer, P.D.; Hilton, M.R.; Bauer, R. Effects of microstructure and adhesion on performance of sputter-deposited MoS_2 solid lubricant coatings. *Mech. Coat. Tribol. Ser.* **1990**, *17*, 121–128. [CrossRef]

16. Tillmann, W.; Wittig, A.; Stangier, D.; Thomann, C.-A.; Moldenhauer, H.; Debus, J.; Aurich, D.; Brümmer, A. Investigation of the Tribofilm Formation of HiPIMS Sputtered MoSx Thin Films in Different Environments by Raman Scattering. *Lubricants* **2019**, *7*, 100. [CrossRef]

17. Li, Y.; Xie, M.; Sun, Q.; Xu, X.; Fan, X.; Zhang, G.; Li, H.; Zhu, M. The effect of atmosphere on the tribological behavior of magnetron sputtered MoS_2 coatings. *Surf. Coat. Technol.* **2019**, *378*, 125081. [CrossRef]

18. Aubert, A.; Nabot, J.P.; Ernoult, J.; Renaux, P. Preparation and properties of MoSx films grown by d.c. magnetron sputtering. *Surf. Coat. Technol.* **1990**, *41*, 127–134. [CrossRef]

19. Bülbül, F.; Efeoğlu, İ. Synergistic effect of bias and target currents for magnetron sputtered MoS_2-Ti composite films. *Mater. Test.* **2016**, *58*, 471–474. [CrossRef]

20. Vierneusel, B.; Tremmel, S.; Wartzack, S. Effects of deposition parameters on hardness and lubrication properties of thin MoS 2 films. *Materialwiss. Werkst.* **2012**, *43*, 1029–1035. [CrossRef]

21. Bellido-González, V.; Jones, A.H.S.; Hampshire, J.; Allen, T.J.; Witts, J.; Teer, D.G.; Ma, K.J.; Upton, D. Tribological behaviour of high performance MoS_2 coatings produced by magnetron sputtering. *Surf. Coat. Technol.* **1997**, *97*, 687–693. [CrossRef]

22. Serpini, E.; Rota, A.; Ballestrazzi, A.; Marchetto, D.; Gualtieri, E.; Valeri, S. The role of humidity and oxygen on MoS_2 thin films deposited by RF PVD magnetron sputtering. *Surf. Coat. Technol.* **2017**, *319*, 345–352. [CrossRef]

23. Zhang, X.; Qiao, L.; Chai, L.; Xu, J.; Shi, L.; Wang, P. Structural, mechanical and tribological properties of Mo–S–N solid lubricant films. *Surf. Coat. Technol.* **2016**, *296*, 185–191. [CrossRef]

24. Hilton, M.R.; Bauer, R.; Didziulis, S.V.; Dugger, M.T.; Keem, J.M.; Scholhamer, J. Structural and tribological studies of MoS_2 solid lubricant films having tailored metal-multilayer nanostructures. *Surf. Coat. Technol.* **1992**, *53*, 13–23. [CrossRef]

25. Roberts, E.W.; Williams, B.J.; Ogilvy, J.A. The effect of substrate surface roughness on the friction and wear of sputtered MoS_2 films. *J. Phys. D Appl. Phys.* **1992**, *25*, A65–A70. [CrossRef]

26. Wong, W.C.; Ng, S.M.; Wong, H.F.; Cheng, W.F.; Mak, C.L.; Leung, C.W. Effect of post-annealing on sputtered MoS_2 films. *Solid State Electron.* **2017**, *138*, 62–65. [CrossRef]

27. Gilmore, R.; Baker, M.A.; Gibson, P.N.; Gissler, W.; Stoiber, M.; Losbichler, P.; Mitterer, C. Low-friction TiN–MoS_2 coatings produced by dc magnetron co-deposition. *Surf. Coat. Technol.* **1998**, *108-109*, 345–351. [CrossRef]

28. Amaro, R.I.; Martins, R.C.; Seabra, J.O.; Renevier, N.M.; Teer, D.G. Molybdenum disulphide/titanium low friction coating for gears application. *Tribol. Int.* **2005**, *38*, 423–434. [CrossRef]

29. Sun, L.; Ruan, T.; Yuan, Z.; Fang, Q.; Gong, W.; Wu, X.; Mei, S. Microstructures and properties of Mo2N+MoS_2 coatings deposited by direct current magnetron sputtering. *Vacuum* **2020**, *177*, 109406. [CrossRef]

30. Zhang, R.; Cui, Q.; Weng, L.; Sun, J.; Hu, M.; Fu, Y.; Wang, D.; Jiang, D.; Gao, X. Modification of structure and wear resistance of closed-field unbalanced-magnetron sputtered MoS_2 film by vacuum-heat-treatment. *Surf. Coat. Technol.* **2020**, 126215. [CrossRef]

31. Ehiasarian, A.P.; Vetushka, A.; Hecimovic, A.; Konstantinidis, S. Ion composition produced by high power impulse magnetron sputtering discharges near the substrate. *J. Appl. Phys.* **2008**, *104*, 83305. [CrossRef]

32. Lewin, E.; Loch, D.; Montagne, A.; Ehiasarian, A.P.; Patscheider, J. Comparison of Al–Si–N nanocomposite coatings deposited by HIPIMS and DC magnetron sputtering. *Surf. Coat. Technol.* **2013**, *232*, 680–689. [CrossRef]

33. Kamath, G.; Ehiasarian, A.P.; Purandare, Y.; Hovsepian, P.E. Tribological and oxidation behaviour of TiAlCN/VCN nanoscale multilayer coating deposited by the combined HIPIMS/(HIPIMS-UBM) technique. *Surf. Coat. Technol.* **2011**, *205*, 2823–2829. [CrossRef]

34. Ehiasarian, A.P.; Münz, W.-D.; Hultman, L.; Helmersson, U.; Petrov, I. High power pulsed magnetron sputtered CrNx films. *Surf. Coat. Technol.* **2003**, *163*, 267–272. [CrossRef]

35. Bobzin, K.; Brögelmann, T.; Kruppe, N.C.; Basturk, S.; Klocke, F.; Mattfeld, P.; Trauth, D.; Hild, R. Synthesis, characterization, and tribological evaluation of HPPMS ($Cr_{1-x}Al_x$)N + MoS_y coatings. *Surf. Coat. Technol.* **2016**, *308*, 383–393. [CrossRef]

36. Moldenhauer, H.; Wittig, A.; Kokalj, D.; Stangier, D.; Brümmer, A.; Tillmann, W.; Debus, J. Resonant Raman scattering characterization of thermally annealed HiPIMS deposited MoS coatings. *Surf. Coat. Technol.* **2019**, *377*, 124891. [CrossRef]

37. Tillmann, W.; Wittig, A.; Stangier, D.; Moldenhauer, H.; Thomann, C.-A.; Debus, J.; Aurich, D.; Bruemmer, A. Influence of the bias-voltage, the argon pressure and the heating power on the structure and the tribological properties of HiPIMS sputtered MoSx films. *Surf. Coat. Technol.* **2020**, *385*, 125358. [CrossRef]

38. Arslan, E.; Baran, Ö.; Efeoglu, I.; Totik, Y. Evaluation of adhesion and fatigue of MoS_2–Nb solid-lubricant films deposited by pulsed-dc magnetron sputtering. *Surf. Coat. Technol.* **2008**, *202*, 2344–2348. [CrossRef]

39. Debus, J.; Schindler, J.J.; Waldkirch, P.; Goeke, S.; Brümmer, A.; Biermann, D.; Bayer, M. Indication of worn WC/C surface locations of a dry-running twin-screw rotor by the oxygen incorporation in tungsten-related Raman modes. *Appl. Phys. Lett.* **2016**, *109*, 171601. [CrossRef]

40. Siu, K.W.; Ngan, A.H.W. The continuous stiffness measurement technique in nanoindentation intrinsically modifies the strength of the sample. *Philos. Mag.* **2013**, *93*, 449–467. [CrossRef]

41. Oliver, W.C.; Pharr, G.M. An improved technique for determining hardness and elastic modulus using load and displacement sensing indentation experiments. *J. Mater. Res.* **1992**, *7*, 1564–1583. [CrossRef]

42. Woo, S.; Park, H.C.; Son, Y.-W. Poisson's ratio in layered two-dimensional crystals. *Phys. Rev. B* **2016**, *93*, 543. [CrossRef]

43. Papa, F.; Gerdes, H.; Bandorf, R.; Ehiasarian, A.P.; Kolev, I.; Braeuer, G.; Tietema, R.; Krug, T. Deposition rate characteristics for steady state high power impulse magnetron sputtering (HIPIMS) discharges generated with a modulated pulsed power (MPP) generator. *Thin Solid Films* **2011**, *520*, 1559–1563. [CrossRef]

44. Alami, J.; Sarakinos, K.; Mark, G.; Wuttig, M. On the deposition rate in a high power pulsed magnetron sputtering discharge. *Appl. Phys. Lett.* **2006**, *89*, 154104. [CrossRef]

45. Lauwerens, W.; Wang, J.; Navratil, J.; Wieërs, E.; D'haen, J.; Stals, L.M.; Celis, J.P.; Bruynseraede, Y. Humidity resistant MoSx films prepared by pulsed magnetron sputtering. *Surf. Coat. Technol.* **2000**, *131*, 216–221. [CrossRef]

46. Chromik, S.; Rosová, A.; Dobročka, E.; Kobzev, A.P.; Hulman, M.; Sojkova, M.; Hutár, P.; Machajdík, D. MoS_2 thin films prepared by sulfurization. In Proceedings of the Nanoengineering, Fabrication, Properties, Optics, and Devices XIV. Nanoengineering: Fabrication, Properties, Optics, and Devices XIV, San Diego, CA, USA, 6–10 August 2017; SPIE Press: Bellingham, WA, USA, 2017; p. 56, ISBN 9781510611658.

47. Shafi, P.M.; Bose, A.C. Impact of crystalline defects and size on X-ray line broadening: A phenomenological approach for tetragonal SnO_2 nanocrystals. *AIP Adv.* **2015**, *5*, 57137. [CrossRef]

48. Ingham, B.; Toney, M.F. X-ray diffraction for characterizing metallic films. In *Metallic Films for Electronic, Optical and Magnetic Applications: Structure, Processing and Properties*; Barmak, K., Coffey, K., Eds.; Woodhead Publishing Limited: Oxford, UK, 2014; pp. 3–38. ISBN 9780857090577.

49. Lüth, H. *Solid Surfaces, Interfaces and Thin Films*; Springer: Berlin/Heidelberg, Germany, 2010; ISBN 9783642135910.

50. Goloveshkin, A.S.; Bushmarinov, I.S.; Lenenko, N.D.; Buzin, M.I.; Golub, A.S.; Antipin, M.Y. Structural Properties and Phase Transition of Exfoliated-Restacked Molybdenum Disulfide. *J. Phys. Chem. C* **2013**, *117*, 8509–8515. [CrossRef]

51. Mignuzzi, S.; Pollard, A.J.; Bonini, N.; Brennan, B.; Gilmore, I.S.; Pimenta, M.A.; Richards, D.; Roy, D. Effect of disorder on Raman scattering of single-layer MoS$_2$. *Phys. Rev. B* **2015**, *91*. [CrossRef]

52. Placidi, M.; Dimitrievska, M.; Izquierdo-Roca, V.; Fontané, X.; Castellanos-Gomez, A.; Pérez-Tomás, A.; Mestres, N.; Espindola-Rodriguez, M.; López-Marino, S.; Neuschitzer, M.; et al. Multiwavelength excitation Raman scattering analysis of bulk and two-dimensional MoS$_2$: Vibrational properties of atomically thin MoS$_2$ layers. *2D Mater.* **2015**, *2*, 35006. [CrossRef]

53. Molina-Sánchez, A.; Wirtz, L. Phonons in single-layer and few-layer MoS$_2$ and WS$_2$. *Phys. Rev. B* **2011**, *84*, 155413. [CrossRef]

54. Najmaei, S.; Liu, Z.; Ajayan, P.M.; Lou, J. Thermal effects on the characteristic Raman spectrum of molybdenum disulfide (MoS$_2$) of varying thicknesses. *Appl. Phys. Lett.* **2012**, *100*, 13106. [CrossRef]

55. Qian, Q.; Zhang, Z.; Chen, K.J. In Situ Resonant Raman Spectroscopy to Monitor the Surface Functionalization of MoS$_2$ and WSe$_2$ for High-k Integration: A First-Principles Study. *Langmuir* **2018**, *34*, 2882–2889. [CrossRef]

56. Vierneusel, B.; Schneider, T.; Tremmel, S.; Wartzack, S.; Gradt, T. Humidity resistant MoS$_2$ coatings deposited by unbalanced magnetron sputtering. *Surf. Coat. Technol.* **2013**, *235*, 97–107. [CrossRef]

57. Gao, F.M.; Gao, L.H. Microscopic models of hardness. *J. Superhard Mater.* **2010**, *32*, 148–166. [CrossRef]

58. Sharma, K.K.; Sharma, L.K. *A Textbook of Physical Chemistry. For BSc Students of All Indian Universities under CBCS*, 6th ed.; Vikas Publishing House: Noida, India, 2016; ISBN 9352590422.

59. Zhang, S. *Nanostructured Thin Films and Coatings. Mechanical Properties*; CRC Press: Hoboken, NJ, USA, 2010; ISBN 9781420094022.

60. Zhang, X.; Vitchev, R.G.; Lauwerens, W.; Stals, L.; He, J.; Celis, J.-P. Effect of crystallographic orientation on fretting wear behaviour of MoSx coatings in dry and humid air. *Thin Solid Films* **2001**, *396*, 69–77. [CrossRef]

61. Didziulis, S.V.; Fleischauer, P.D.; Soriano, B.L.; Gardos, M.N. Chemical and tribological studies of MoS$_2$ films on SiC substrates. *Surf. Coat. Technol.* **1990**, *43–44*, 652–662. [CrossRef]

62. Lundin, D.; Minea, T.; Gudmundsson, J.T. (Eds.) *High Power Impulse Magnetron Sputtering. Fundamentals, Technologies, Challenges and Applications*; Elsevier: Amsterdam, The Netherlands, 2020; ISBN 0128124547.